Mitigating Aerodynamic Interference at the Blade-to-Rotor Arm Connection in Darrieus VAWTs

Journal of Physics: Conference Series **3224** (2026) 092019 doi:10.1088/1742-6596/3224/9/092019

Mitigating Aerodynamic Interference at the Blade-to-Rotor Arm Connection in Darrieus VAWTs

L Calzoni[1], X Liu[2], L Manfriani[2] and A Croce[1]

[1]Department of Aerospace Science and Technology, Politecnico di Milano, Milan, Italy
[2]School of Engineering, Centre for Aviation, Winterthur, Switzerland

E-mail: lucrezia.calzoni@polimi.it

Abstract. This study investigates aerodynamic interference at the blade-to-rotor arm junction of a pitch-controlled Darrieus-type Vertical Axis Wind Turbine (VAWT). Wind tunnel measurements of a scaled model revealed non-zero lift offset at $\alpha = 0°$ despite using symmetric airfoils. Through RANS simulations and volumetric flow visualizations, this junction-induced behavior was traced to asymmetric separation and a low-velocity deficit that expands preferentially on the pressure side due to the bluff-body influence of the rotor arm. Two mitigation strategies, root-gap sealing and aerodynamic fences, effectively suppressed spanwise flow migration and restored pressure distribution at the blade root. Experiments demonstrate that combining these modifications doubles the integral lift coefficient and reduces parasitic drag by 33%. These results demonstrate that targeted junction modifications can substantially improve VAWT efficiency, offering guidelines for optimizing the aerodynamic integration of rotor components.

1. Introduction and Motivations

Wind energy is a mature renewable technology dominated by Horizontal-Axis Wind Turbines (HAWTs), which have been extensively optimized for high-efficiency onshore and offshore applications. In contrast, Vertical-Axis Wind Turbines (VAWTs) offer distinct advantages in complex, space-constrained environments, such as gusty urban sites and high-density arrays, where their omni-directional capability and lower center of gravity are particularly beneficial [1].

Despite their potential, VAWTs have received comparatively less research attention, particularly regarding local aerodynamic integration. Most contemporary studies, such as that by Shubham [2], focus on full-rotor performance and global wake characteristics. While these works evaluate how design modifications impact overall power output, they often rely on simplified rotor representations that overlook the fine-scale geometric details at the blade-to-arm interface.

Consequently, the blade-to-rotor arm connection remains an underexplored zone. This junction is critical because it experiences strong aerodynamic interference and complex vortex structures that can lead to elevated fatigue loads, potential structural issues, and efficiency losses. Although high-fidelity Computational Fluid Dynamics (CFD) simulations of complete rotors often capture large-scale vortex generation at these junctions, the underlying mechanisms and possible mitigation strategies are rarely isolated and analyzed in detail.

The present study addresses this gap by investigating the aerodynamic behavior at the blade-to-rotor arm connection of a pitch-controlled Darrieus-type VAWT. Initial wind tunnel tests revealed that, despite the use of symmetric airfoils, the blades generate non-zero lift at

$\alpha = 0°$. This observation indicates the presence of junction-induced aerodynamic asymmetry that compromises spanwise efficiency.

To isolate these effects, the present analysis examines the blade–arm junction in a static, high-resolution approach, highlighting blade–housing interactions that are typically masked in global rotor studies. While in real VAWT operation these local interference effects would superimpose with the well-known virtual camber effect associated with curved blade rotation, the present approach intentionally isolates the junction mechanisms in order to characterize their aerodynamic impact and to begin evaluating potential mitigation strategies.

By combining experimental flow visualization and CFD simulations, this study aims to: (i) clarify the flow mechanisms responsible for these parasitic junction effects and (ii) evaluate design modifications capable of mitigating them and improving blade aerodynamic performance. Rather than providing a purely numerical benchmark, this work offers preliminary design-oriented insights for managing the complex junction flows inherent in advanced VAWT architectures, thus supporting the development of more efficient and reliable turbine technologies.

The remainder of this paper is organized as follows: Section 2 describes the experimental setup, while Section 3 presents the numerical framework. Section 4 discusses the aerodynamic results and the effectiveness of the proposed mitigation strategies. Finally, Section 5 summarizes the conclusions and design recommendations.

2. Experimental Setup

2.1. Experimental Facility and Model Geometry

Experiments were conducted in the ALFA low-speed wind tunnel at the ZHAW Centre for Aviation (Switzerland). This closed-loop facility features an octagonal test section (1.2 m x 0.9 m x 0.6 m) that provides high-quality flow with turbulence intensities below 0.5%. As shown in Figure 1a, the model represents a pitch-controlled Darrieus-type VAWT blade-to-rotor arm connection and consists of two main components: the rotor arm with an integrated pitch-housing and the blades.

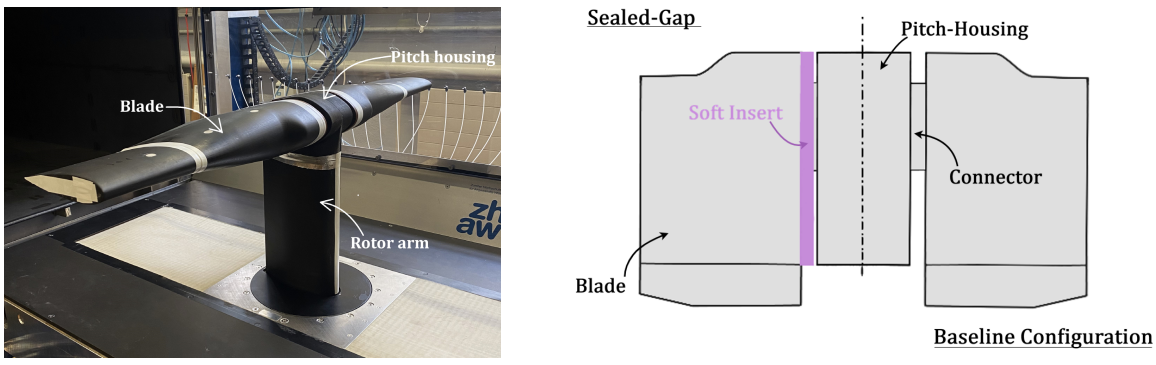

(a) **(b)**

Figure 1. 3D-printed blade-to-rotor arm scaled model installed in the ALFA test section **(a)** and schematic top view comaparison between the baseline and the sealed-gap configuration **(b)**.

The blades feature a tapered planform with a spanwise thickness distribution optimized for structural and aerodynamic performance. At the root, thick flatback airfoils ($t/c = 40 - 45\%$) featuring truncated trailing edges and an offset cavity are employed. Moving toward the tip, blade thickness decreases, transitioning to conventional sharp-trailing-edge symmetric

profiles. All airfoil sections are geometrically symmetric about the chord line to ensure balanced aerodynamic behavior throughout the rotor's rotation. Although the experimental model does not represent the full blade span, the selected portion captures the complete transition from root to tip profile, ensuring accurate characterization of local aerodynamic behavior and spanwise gradients.

The rotor arm connects to the blade via the pitch housing, which contains the pitch adjustment mechanism. This housing is faired as a thick airfoil at the blade-connection side and is coupled to the blade through a cylindrical structural connector. This arrangement creates a root gap and a complex junction which constitute the primary focus of the present study. Finally, all external surfaces were finished with a uniform matte black coating to minimize optical reflections for the Probe Capture (ProCap) flow-visualization system [3].

2.2. Experimental Configurations

To identify the physical drivers of the observed lift offset at $\alpha = 0°$ and explore potential aerodynamic improvements, the experimental investigation followed an incremental three-stage approach:

I. Baseline Configuration: The unmodified geometry, featuring an open gap and exposed cylindrical connector between the blade root and pitch-housing, served as a reference to quantify inherent bluff-body interference and junction effects (Figure 1b, right side).

II. Sealed-Gap Configuration: The root gap was sealed with an airfoil-conforming soft insert (Figure 2a, left side), shielding the internal connector from the freestream. This isolates the impact of internal-gap flow separation and evaluates the potential for performance recovery associated with improved surface continuity.

III. Fenced Configurations: To mitigate persistent spanwise flow observed even with a sealed gap, thin aluminum fences were installed at the blade root (Figure 2b). These fences act as physical barriers to promote a quasi-two-dimensional flow field. Three sub-configurations, suction-side, pressure-side, and bilateral fences, were evaluated to assess local flow sensitivity.

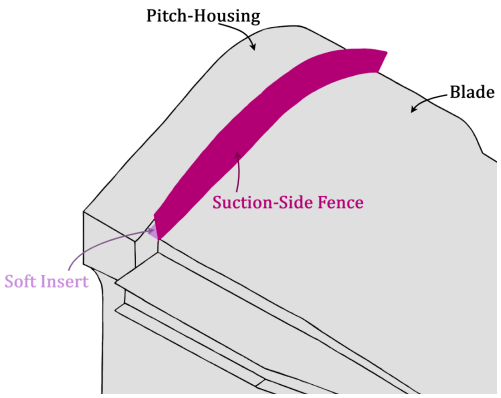

(a) Suction-side fence.

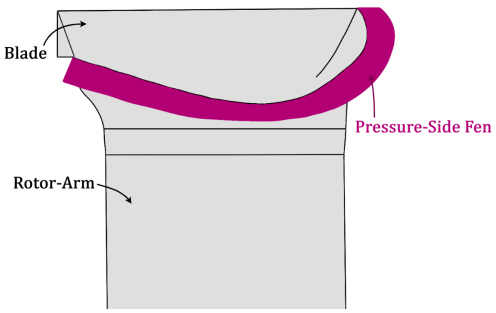

(b) Pressure-side fence (side view).

Figure 2. Schematic of the Fenced configurations, with the bilateral case featuring fences on both suction and pressure sides.

2.3. Model Installation and Measurements

To leverage the wind tunnel's automated test cart for angle-of-attack (α) adjustments, the model was mounted with a 90° rotation relative to its real-world orientation (Figure 1a). In this configuration, the model spans the full test section width with a tip clearance of less than 1 mm, causing the wind tunnel walls to act as natural splitter plates, following Selig et al.[4]. This

arrangement enables static characterization of blade-housing interactions rather than replicating full rotational dynamics.

The internal architecture was specifically engineered to decouple aerodynamic loads and isolate blade–housing interference. A central sting supports a rigid steel frame, while an internal beam carries the blades through a precision-machined hole matrix for discrete pitch adjustments. To ensure measurement purity, the external 3D-printed shells, representing the pitch-housing and rotor surfaces, were mounted to the internal skeleton without making physical contact with the blade-support beam. This nested architecture enables a dual-measurement strategy (Figure 3):

- **Local Blade Loads:** Captured by an ATI Mini45 six-axis balance integrated within the internal frame. By isolating loads transmitted through the blade-support beam, the balance records the local blade loading as influenced by junction-induced interference.
- **Global System Loads:** Measured by a RUAG 798-6C six-axis balance at the sting base, recording the total aerodynamic loads of the entire assembly, including the integrated contributions of the blades, pitch-housing, and rotor arm.

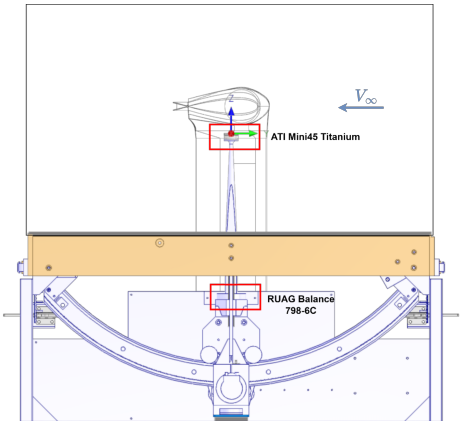

Figure 3. Side view of the dual-balance setup.

2.4. Test Conditions and Data Acquisition

Measurements were conducted across a freestream velocity range of 18 m/s to 30 m/s, with primary analysis focused on the 22 m/s case ($Re_c = 2.3 \times 10^5$) for consistency with numerical simulations. At these Reynolds numbers, to ensure predictable boundary layer behavior and suppress laminar separation bubbles, transition was enforced using trip dots following Braslow et al.[5]. Aerodynamic loads were acquired during a quasi-steady pitching sequence from $\alpha = -12°$ to $+12°$ in $0.1°$ increments at 100 Hz. As a first step, the present analysis focuses specifically on $\alpha = 0°$, providing a fundamental benchmark that allows junction-induced aerodynamic interference to be studied in isolation, without contributions from incidence-driven lift. Given the high blockage ratio (13.3%), all data were rigorously corrected for solid and wake blockage using the methodology described by Pope at al.[6], with the corrections validated against high-fidelity CFD simulations.

Flow-field characterization was performed using the Probe Capture (ProCap) system [3], providing real-time volumetric visualization of the aerodynamic environment. This "scan-and-paint" approach integrates a 14-hole iProbe with infrared optical tracking to reconstruct three-dimensional velocity structures within a defined measurement volume. All scans were conducted at a reduced freestream velocity of 10 m/s to ensure probe-handling stability. While this velocity is lower than the 22 m/s speed used in CFD simulations, simultaneous integral force measurements confirmed that the aerodynamic trends and junction-induced interference mechanism remain representative. Consequently, ProCap data serve in this study as a qualitative verification tool of flow topology rather than as a quantitative magnitude comparison.

3. Numerical Methodology

3.1. Solver Configuration

Three-dimensional steady-state incompressible Reynolds-Averaged Navier–Stokes (RANS) simulations were performed using ANSYS Fluent 2022R2, employing a pressure-based formulation suitable for low-Mach-number conditions. Turbulence closure was provided by the Menter k-ω SST model [7], selected for its proven ability to capture boundary-layer behavior and flow separation under adverse pressure gradients. Pressure–velocity coupling was handled using the COUPLED algorithm to ensure stable convergence in regions of high pressure gradients.

3.2. Computational Domains and Boundary Conditions

To rigorously evaluate aerodynamic forces and decouple interference effects, three distinct computational domains were defined. In all configurations, the blade was set at a fixed pitch angle of 0° and geometric symmetry about xy-plane was exploited to halve the computational domain, reducing computational cost without compromising accuracy. Boundary conditions remained consistent across all domains: a uniform inlet velocity of 22 m/s ($Re = 2.3 \times 10^5$) with a low turbulence intensity (1%), and a static pressure of 0 Pa at the outlet. No-slip conditions were enforced on all solid surfaces.

The first two domains were designed to evaluate wall confinement effects. The Wind Tunnel (WT) domain replicates the physical facility's cross-section, where the high blockage ratio of 13.3% leads to significant wall-induced flow acceleration. To isolate and quantify this effect, a second Open Field (OF) domain ($12 \times 6 \times 8$ m) was created to simulate quasi-free-stream conditions with negligible blockage ($\approx 0.15\%$). Comparing aerodynamic results between the WT and OF domains quantifies the local velocity increase due to wall proximity and provides a numerical benchmark for the blockage correction methods applied to the experimental data. Finally, a Blade-Only (BO) domain was developed to isolate aerodynamic interference at the blade root caused by the pitch-housing. Since testing an isolated 3D blade was physically impractical in the adopted experimental setup, this numerical configuration retains the WT domain dimensions but excludes the rotor arm and pitch-housing. It provides a critical baseline for characterizing the isolated blade's performance and disentangling complex interactions between rotor components and the blade.

3.3. Mesh Strategy and Grid Independence

Unstructured meshes were generated using ANSYS Meshing to resolve the complex geometry, including the offset cavity and pitch-housing. Near-wall resolution employed 30 prism inflation layers (growth rate of 1.1 and first-layer height of $\approx 3.32 \times 10^{-5}$ m) targeting an area-weighted $y^+ \approx 1$, ensuring proper resolution of the viscous sublayer for the k-ω SST turbulence model (Figure 4a). Additional inflation layers were applied to the WT domain enclosure walls to reproduce physical boundary layer development.

Surface meshes were refined in high-curvature regions, such as the leading and trailing edges, with a maximum expansion ratio of 1.1 and a minimum of 300 divisions per airfoil. In the OF domain, the wake was resolved using three nested Body Of Influence (BOI) zones (Figure 4b) with progressively coarsening maximum element sizes (0.02 m, 0.065 m, and 0.09 m). To maintain consistent resolution in both the blade and near-wake regions for comparative analysis, the WT and BO domains were meshed using only the small (BOI 1) and medium (BOI 2) BOI zones of the Open Field configuration.

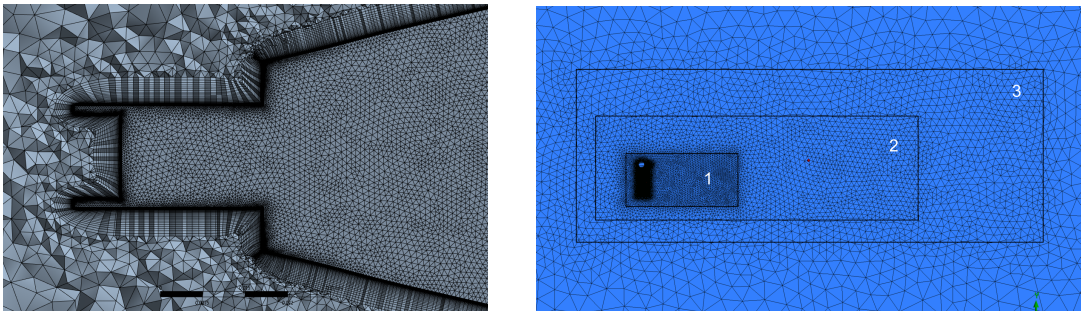

(a) **(b)**

Figure 4. Close-up of the inflation layer structure within the airfoil offset cavity **(a)** and computational grid of the Open Field domain with the three BOI **(b)**.

A four-level grid refinement study was conducted for each domain, with global cell count ranging from roughly 14 to 33 million elements. Global convergence was assessed using the integrated lift (C_L) and drag (C_D) coefficients with the selected mesh (Mesh 3) showing negligible variations (below 0.1% for C_L and 0.3% for C_D) compared to the finest grid. Local solution accuracy was also verified through spanwise pressure distributions at multiple spanwise location, with a L^2 error norm on the order of 10^{-4}. Final mesh characteristics for each domain are detailed in Table 1.

Table 1. Key mesh characteristics for the three computational domains.

Domain	Wind Tunnel (WT)	Open Field (OF)	Blade-Only (BO)
Global Cell Counts	26138065	30413806	22194407
Max Skewness	0.89	0.83	0.76
Min Orthogonal Quality	0.204	0.216	0.25

3.4. Experimental Validation

To ensure consistency with experimental conditions, the WT domain CFD results were compared against wind tunnel measurements at $\alpha \in \{-2°, 0°, 2°\}$. The lift coefficient is predicted with good accuracy, with differences remaining below $\Delta C_L \approx 0.015$ across the tested angles of attack. The drag coefficient shows slightly larger deviations, remaining under $\Delta C_D \approx 0.0023$, which is typical for steady RANS simulations of thick flatback airfoils where unsteady wake structures are not fully resolved. Despite this, the CFD accurately reproduces the relative variations in lift, drag, and efficiency across configurations, ensuring that the key aerodynamic trends relevant to junction-induced interference and mitigation strategies are correctly captured in this preliminary study.

4. Results and Discussion

4.1. Characterization of Aerodynamic Interference

Initial experimental characterization of the baseline configuration revealed a clear deviation from classical aerodynamic behavior. Although the blade is composed entirely of symmetric airfoil sections, integrated load measurements from the internal balance recorded a non-zero lift coefficient at $\alpha = 0°$. Since symmetric airfoils, including flatback profiles, should generate zero lift in a uniform stream, this indicates the presence of system-level aerodynamic interference. To identify the drivers of this lift offset, CFD simulations comparing the Wind Tunnel (WT) domain with the isolated Blade-Only (BO) domain were analyzed.

The most pronounced difference between the two cases appears in the sectional lift coefficient (C_l). As illustrated in Figure 5a, the isolated blade maintains $C_l \approx 0$ along the entire span, whereas the full model exhibits a pronounced lift peak at the root, followed by a rapid decay toward the tip.

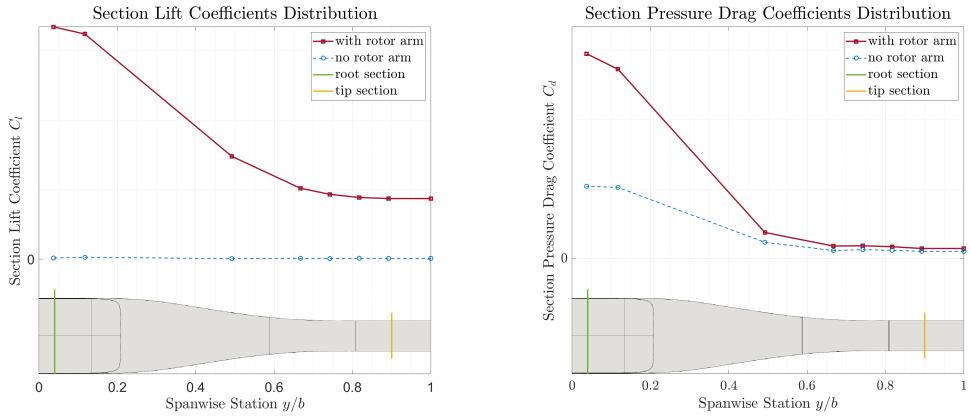

(a) **(b)**

Figure 5. Spanwise distributions of **(a)** sectional lift coefficient (C_l) and **(b)** pressure drag coefficient ($C_{d,p}$) at $\alpha = 0°$. Both plots use the same y-axis scale for direct comparison.

This localized effect is further confirmed by spanwise pressure coefficient (C_p) distributions. At 4% span, near the blade-connector junction, the full model C_p profile deviates significantly from that of the isolated blade (Figure 6a), showing a pressure imbalance between the suction and pressure sides. Conversely, at 90% span, the C_p distribution resembles that of the isolated blade solution (Figure 6b), confirming that the interference is confined primarily to the junction region.

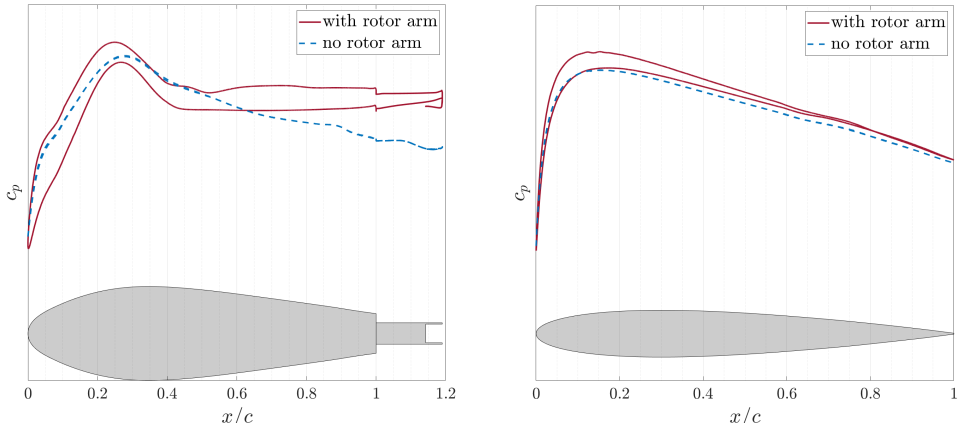

(a) Root section (≈ 4% span). **(b)** Tip section (≈ 90% span).

Figure 6. Sectional pressure coefficient (C_p) distributions at $\alpha = 0°$: comparison between the isolated blade and full assembly. The sections considered are shown for ease of reference in Figure 5.

Root-section flow topology provides further insight into the mechanisms driving this interference induced lift. At the root, the full model exhibits a pronounced C_p plateau extending over more than 40% of the chord (Figure 6a), indicative of severe flow separation. Wall shear stress (WSS) and Line Integral Convolution (LIC) surface visualizations confirm that this plateau

corresponds to extended regions of near-zero WSS on both blade surfaces. While separation occurs on both sides, the footprint is substantially larger on the pressure side, as evidenced by the divergent limiting streamline patterns highlighted in green in Figure 7. Comparison with the isolated blade (Figure 7) confirms that these features are purely interference-driven, arising from the connection to the pitch housing rather than the blade geometry itself.

This asymmetric separation non-uniformly thickens the boundary layer, producing a displacement thickness imbalance between the suction and pressure sides. Consequently, the external flow perceives an effective camber-like asymmetry, redistributing surface pressures and generating lift at $\alpha = 0°$. Unlike the virtual camber effect associated with rotating blades, this phenomenon results directly from the asymmetric blockage induced by the pitch-housing and rotor arm, which forces a larger separation zone on the pressure side (Figure 7).

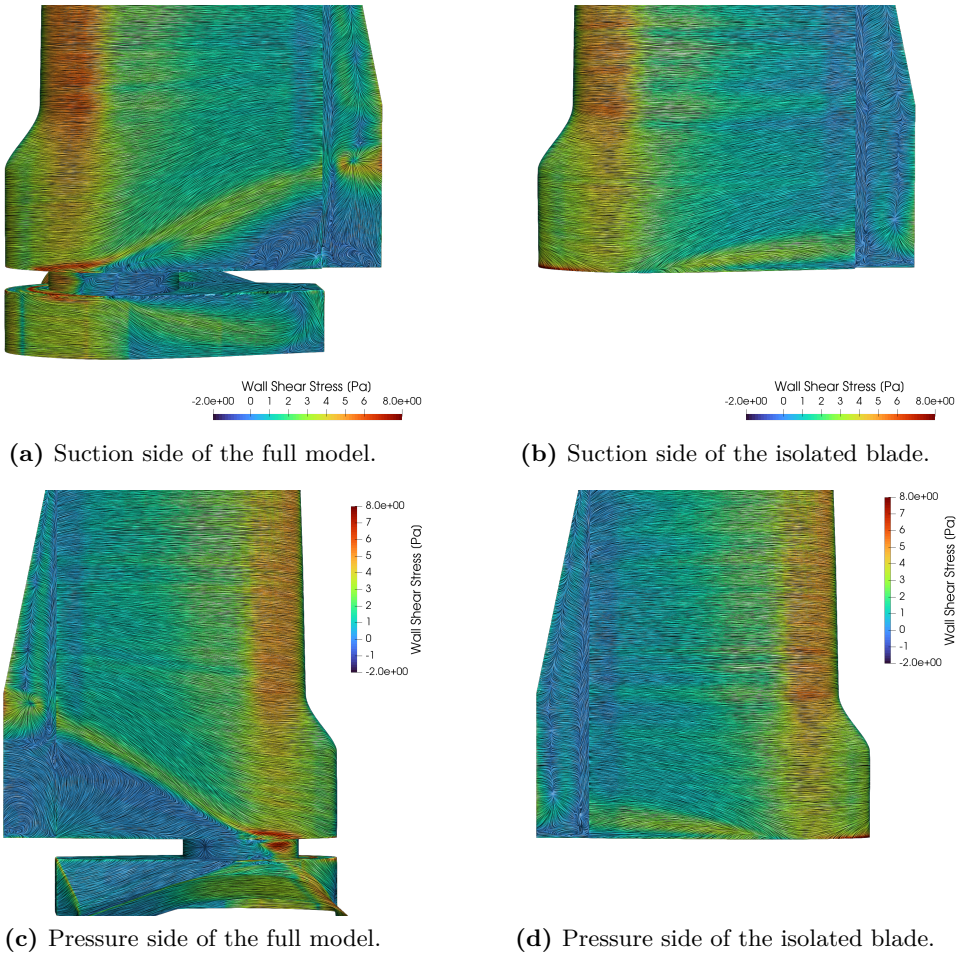

(a) Suction side of the full model. **(b)** Suction side of the isolated blade.

(c) Pressure side of the full model. **(d)** Pressure side of the isolated blade.

Figure 7. Surface flow topology at $\alpha = 0°$ showing the impact of pitch-housing interference on wall shear stress and limiting streamlines.

The origin of this asymmetric separation is traced directly to the blade–connector junction, where flow impinging on the cylindrical connector detaches abruptly. This forms a complex, bubble-like separation region characterized by a pair of counter-rotating vortices that merge downstream, generating a highly asymmetric wake (Figure 8). This asymmetry stems from the rotor arm's bluff-body influence, which induces large-scale separation that interacts with the blade-root shear layers. As evidenced by 3D cross-sectional velocity contours (Figure 8b), this interaction forces the low-velocity deficit to expand preferentially on the pressure side.

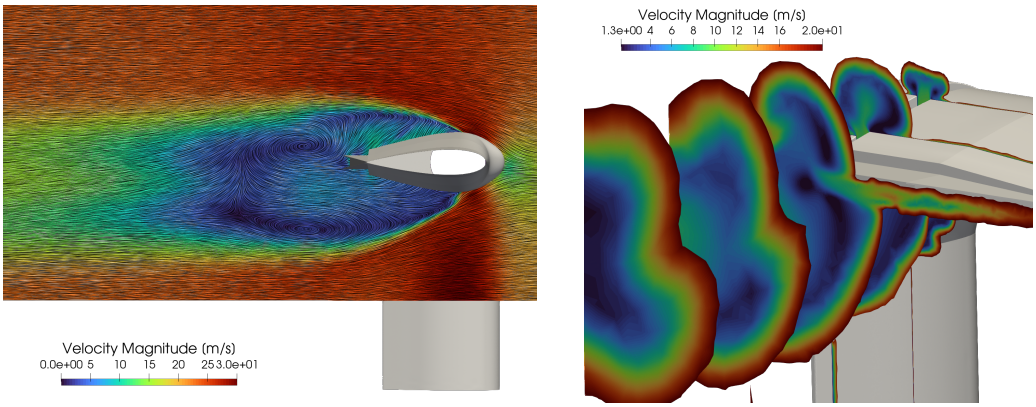

(a) **(b)**

Figure 8. Detailed flow-field topology at $\alpha = 0°$: **(a)** 2D LIC visualization of flow separation within the blade-to-arm junction and **(b)** 3D Velocity iso-contours on cross-sectional slices.

While this junction-induced lift is non-negligible, it represents an inefficient byproduct of the assembly's current configuration. Specifically, sectional pressure drag coefficients ($C_{d,p}$) reveal a substantial increase in form drag concentrated near the blade root, resulting in a marked degradation of local airfoil efficiency (Figure 5b).

4.2. Mitigation Strategies

Guided by the flow topology established in the previous section, two mitigation strategies were experimentally evaluated: (i) sealing the gap between the blade root and the pitch housing, and (ii) introducing aerodynamic fences to limit spanwise propagation of the junction-induced wake.

In contrast to the baseline assessment, which relied primarily on sectional CFD data, the effectiveness of the proposed modifications is evaluated here using integral load measurements, complemented by surface tufts and planar velocity contours extracted from the volumetric flow field acquired with the ProCap system. This combined approach enables a direct assessment of global aerodynamic recovery, quantified through the blade efficiency metric $E = C_L/C_D$.

The first mitigation strategy addressed the clearance between the blade root and the pitch housing by sealing the gap, as described in Section 2. This modification restores surface continuity at the junction, preventing freestream access to the internal cylindrical connector, which in the baseline configuration promotes abrupt flow detachment and the formation of an asymmetric separation bubble. At $\alpha = 0°$, the sealed-gap configuration yields a doubling of the integral lift coefficient and a 13% reduction in drag, resulting in more than a two-fold increase in overall blade aerodynamic efficiency as reported in Figure 10a). All performance metrics are normalized to the baseline configuration (set equal to 1 in the plot) to allow immediate visualization of relative improvement.

Planar velocity contours from ProCap measurements were analyzed to elucidate the origin of these performance gains. The visualizations reveal a substantial contraction of the junction-induced wake compared to the baseline (Figure 9a), with the largest reduction occurring on the suction side of the blade. While localized three-dimensional separation persists, the low-velocity deficit is smaller and shifted toward the trailing edge on the upper surface (Figure 9b). This results in a reduction of the displacement thickness (δ^*) on the suction side at the root, whereas the pressure side remains thickened due to the persistent separation induced by the rotor arm's bluff-body influence. The resulting pressure redistribution and shift of the stagnation point provide a physical explanation for the observed doubling of lift at $\alpha = 0°$. Although ProCap velocity magnitudes differ from the 22 m/s CFD, the overall flow topology, including wake

contraction and separation patterns, remains in excellent qualitative agreement.

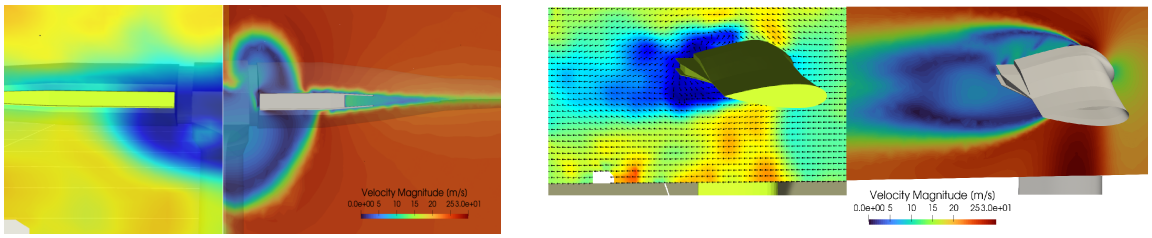

(a) **(b)**

Figure 9. Comparison of the separation zone at $\alpha = 0°$ between sealed-gap ProCap visualizations (left) with baseline CFD results (right) in a transverse plane downstream of the blade **(a)** and in a cross-sectional plane within the connection **(b)**.

In addition, the overall contraction of the wake on both surfaces reduces the momentum thickness of the junction wake, directly correlating with the observed reduction in drag from the integral load measurements. Despite these gains, residual suction-side disturbances persist, indicating that junction-induced flow continues to migrate spanwise, as also highlighted by surface tuft visualizations. This motivates the implementation of aerodynamic fences as a secondary mitigation strategy.

To further mitigate this residual spanwise flow, the effects of aerodynamic fences were evaluated on top of the sealed-gap configuration. Three arrangements were considered: suction-side only, pressure-side only, and bilateral fences, allowing the incremental impact of each arrangement to be assessed.

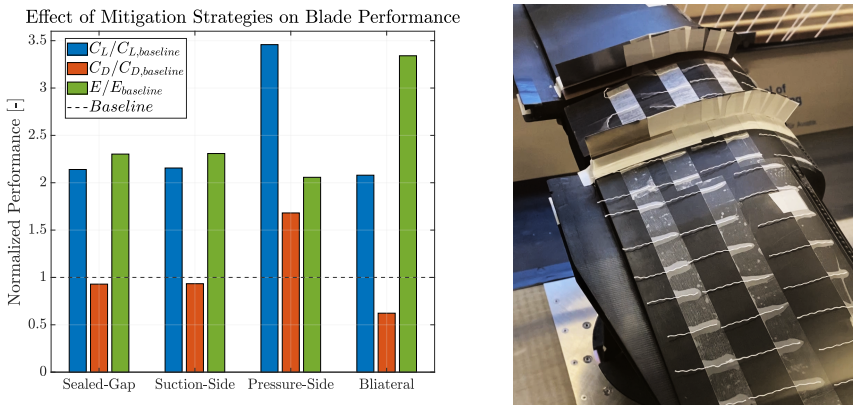

(a) **(b)**

Figure 10. Impact of modifications on normalized integral load performance relative to the baseline **(a)** and surface tuft visualization highlighting the effectiveness of the bilateral fence configuration **(b)**

Unilateral fences did not produce significant performance improvements. A suction-side fence resulted in more locally ordered surface flow, as indicated by tuft alignment, but yielded negligible changes in integral lift and drag coefficients (Figure 10a), suggesting that suction-side disturbances were not the dominant source of remaining parasitic drag. In contrast, a pressure-side fence reduced efficiency by 18% relative to the sealed-gap baseline, primarily due to an increase in drag, highlighting the sensitivity of the root region to asymmetric flow control.

The bilateral fence configuration produced the most pronounced aerodynamic recovery. Integral measurements show a 33% reduction in drag relative to the sealed-gap baseline (Figure 10a),

accompanied by a substantial increase in blade efficiency. Surface tuft visualizations confirm that the dual fences confine the disordered junction flow within the pitch-housing region (Figure 10b), preventing its spanwise migration onto the blade. As a result, the flow remains predominantly chord-wise and attached, closely resembling the isolated-blade behavior observed in blade-only domain.

5. Conclusions

This study characterized and mitigated the aerodynamic interference occurring at the blade-to-rotor arm junction of a pitch-controlled VAWT. Experimental and numerical results revealed that the proximity of the rotor arm induces an asymmetric separation bubble at the blade root, producing an interference effect responsible for a parasitic lift offset at $\alpha = 0°$. An incremental mitigation strategy showed that sealing the root gap partially restores pressure balance, while the addition of bilateral aerodynamic fences effectively suppresses spanwise flow migration and wake contamination. The combined configuration, the bilateral one, achieved a 33% reduction in parasitic drag and doubled the integral lift coefficient (Figure 10a), demonstrating a significant potential for aerodynamic performance recovery. While acknowledging the limitations of the adopted static approach, which isolates junction-induced interference from rotating VAWT aerodynamics and evaluates mitigation strategies only under static conditions and not under the real rotating operation, these findings provide clear preliminary insights for VAWT rotor design. These aspects will be further investigated in future work, where the analysis will account for the additional aerodynamic effects associated with rotor rotation, such as the well-known virtual camber effect. Nevertheless, the present results already suggest useful practical design guidelines. In particular, structural blade-to-arm connectors should be shielded or integrated within a sealed fairing to eliminate open root gaps, which present a primary source of parasitic drag. Bilateral fences at the blade-to-rotor junction help confine disordered flow and maintain predominantly chord-wise, attached flow along the blade. Additionally, designers of active pitch-control systems should account for interference-induced lift offsets in order to optimize power extraction and reduce cyclic fatigue loads. In summary, although the blade-to-rotor arm connection is a structural necessity, its aerodynamic impact is substantial. The strategies demonstrated in this work offer a practical pathway to reduce junction-induced losses, supporting the development of more efficient and reliable VAWTs for urban and high-density applications.

References

[1] Paraschivoiu I, Ammar S and Saeed F 2018 Vawt versus hawt: a comparative performance study of 2–6 mw rated capacity turbines *Transactions of the Canadian Society for Mechanical Engineering* **42** 393–403

[2] Shubham S 2024 *A multi-fidelity approach for aerodynamics and aeroacoustics of vertical axis wind turbines* Ph.D. thesis Nottingham Trent University URL `https://irep.ntu.ac.uk/id/eprint/52000/`

[3] Streamwise gmbh 2026 ProCap: Real-time volumetric flow visualization `https://www.procap.tech` accessed: 2026-01-12

[4] Selig M, Deters R and Williamson G 2011 Wind tunnel testing airfoils at low reynolds numbers

[5] Braslow A L and Knox E C 1958 Simplified method for determination of critical height of distributed roughness particles for boundary-layer transition at mach numbers from 0 to 5 Tech. Rep. NACA-TN-4363 National Advisory Committee for Aeronautics Langley Field, VA URL `https://ntrs.nasa.gov/citations/19930085292`

[6] Barlow J, Rae W and Pope A 1999 *Low-Speed Wind Tunnel Testing* (Wiley) ISBN 9780471557746

[7] Menter F R 1994 Two-equation eddy-viscosity turbulence models for engineering applications *AIAA Journal* **32**